A low-impedance radio-frequency circuit for fast spin manipulations in cold alkali atoms

F. Scazza ✉ iD ; G. Del Pace iD ; L. Pieri iD ; R. Concas iD ; W. J. Kwon iD ; G. Roati iD

Check for updates

View Online

Export Citation

Articles You May Be Interested In

State-dependent transport in RF-dressed atom chip potentials

AVS Quantum Sci. (April 2025)

Numerical simulation and optimization of compact high voltage pulse transformers

AIP Conf. Proc. (September 2022)

AIP Publishing

A low-impedance radio-frequency circuit for fast spin manipulations in cold alkali atoms

F. Scazza,[1,2,3,a] (ID) G. Del Pace,[1,2,4] (ID) L. Pieri,[5] (ID) R. Concas,[2,6] (ID) W. J. Kwon,[1,2,7] (ID) and G. Roati[1,2] (ID)

AFFILIATIONS

[1] Istituto Nazionale di Ottica (CNR-INO), 50019 Sesto Fiorentino, Italy
[2] European Laboratory for Nonlinear Spectroscopy (LENS), 50019 Sesto Fiorentino, Italy
[3] Dipartimento di Fisica, Università degli Studi di Trieste, 34127 Trieste, Italy
[4] Dipartimento di Fisica e Astronomia, Università degli Studi di Firenze, 50019 Sesto Fiorentino, Italy
[5] Radioteknos, 50142 Firenze, Italy
[6] Istituto Italiano di Ricerca Metrologica (INRiM), 10135 Torino, Italy
[7] Department of Physics, Ulsan National Institute of Science and Technology (UNIST), 44919 Ulsan, Republic of Korea

[a] Author to whom correspondence should be addressed: francesco.scazza@units.it

ABSTRACT

We design and implement a low-impedance, high-current radio-frequency (RF) circuit, enabling fast coherent coupling between magnetic levels in cold alkali atomic samples. It is based on a compact, shape-optimized coil that maximizes the RF field coupling with the atomic magnetic dipole, and on coaxial transmission-line transformers that step up the field-generating current flowing in the coil by a factor ~4 to about 7.5 A for 100 W of RF driving. This allows us to obtain a RF coupling field of about $0.035\,\mathrm{G}/\sqrt{\mathrm{W}}$ at the atomic sample location. The system is robust and versatile, as it generates a large RF field without compromising the available optical access, and its central resonant frequency can be adjusted *in situ*. Our approach provides a cost-effective, reliable solution, featuring a negligible level of interference with surrounding electronic equipment thanks to its symmetric layout. We test the circuit performance using a maximum RF power of 80 W at a frequency around 82 MHz, which corresponds to a measured Rabi frequency $\Omega_R/2\pi \simeq 18.5$ kHz, that is, a π-pulse duration of about 27 μs, between two of the lowest states of ^{6}Li at an offset magnetic field of 770 G. Our solution can be readily adapted to other atomic species and vacuum chamber designs, in view of an increasing modularity of cold atom experiments.

I. OVERVIEW

Over the past two decades, the ability to coherently manipulate the internal state of atoms and molecules has proven an essential tool in the field of precision measurements,[1] as well as for the realization of ultracold synthetic matter and atomic quantum simulators of important many-body problems.[2,3] In particular, a key experimental probe of many-body physics in ultracold atomic systems is radio-frequency (RF) spectroscopy,[2,4,5] by which an applied RF pulse is used to transfer atoms from one hyperfine state to another unoccupied state. Addressing the RF transitions that connect hyperfine sub-levels with different interaction properties allows for accessing the spectral properties of elementary excitations in Fermi[6–11] and Bose gases,[12–15] as well as fundamental thermodynamic quantities.[16–18] In this context, a significant demand is the implementation of strong coherent RF drives, which are especially important to precisely trigger and probe non-equilibrium many-body dynamics governed by short-range interactions,[15,18–23] tuned through Feshbach resonances upon varying a static magnetic field applied to the sample. In addition, strong RF driving notably allows for performing efficient evaporation of atomic quantum gases in magnetic traps[24] and for dynamically shaping the trapping potentials.[25,26] It is also becoming increasingly important for realizing fast qubit rotations in atom-based quantum information processing applications.[27,28]

In quantum degenerate Fermi gases, a natural time scale $\tau_F = \hbar/\varepsilon_F$ is set by the Fermi energy ε_F of the system, where $\hbar$ is

the reduced Planck constant $h/2\pi$. The dynamics at short times $t \sim \tau_F$ are expected to be universal, revealing the emergence of elementary excitations in real time,[15,20,22] and serving as a valuable benchmark for many-body theories.[29–31] To experimentally investigate such *ultrafast* dynamics in ultracold Fermi gases, it is necessary to control the spin state of the atoms over time scales on the order of τ_F, whose typical values range between 5 and 50 μs depending on the experimental sample density and atomic mass. The experimental time resolution in controlling the atomic spin state is set by the Rabi frequency Ω_R, characterizing the strength of the coupling between an external electromagnetic (EM) field and the dipole moment associated with the atomic spin. For a given magnetic dipole moment, the only way to increase Ω_R is to increase the amplitude of the driving field experienced by the atoms. At the same time, it is important that the circuit generating the RF field does not perturb the sensitive electronics within the surrounding apparatus. This makes the realization of quiet and efficient RF systems a priority in cold atom laboratories. Moreover, as experimental setups become more complex, including large-aperture imaging systems and multiple laser beams, critical space constraints call for unobtrusive and versatile RF circuit designs.

Here we present the design and implementation of a flexible, compact, and low-cost high-current circuit for efficiently coupling a large RF magnetic field to the spin of alkali atoms, whose transitions within the ground-state manifold typically lie in the 10–200 MHz range, allowing for spin manipulations with $\Omega_R \sim \varepsilon_F/\hbar$. Significant complexity results from the fact that atomic samples are trapped inside an often metallic, ultra-high vacuum chamber by laser light potentials, and are subject to a strong static magnetic field B_0 produced by Feshbach electromagnets. Fulfilling all design requirements, the realized system shows an excellent electronic performance, in agreement with simulations. It has been tested in a typical application case by driving the transition between two ground-state magnetic sublevels of lithium atoms, characterized by a frequency $\nu_0 \simeq 82$ MHz. Moreover, it features a very low level of interference with nearby laboratory electronic equipment, as demonstrated by observed near-unity π-pulse efficiencies even at 100 W-level RF driving and an estimated static B-field fractional stability of about 10^{-5} for $B_0 \simeq 770$ G over several minutes of low-power RF driving with a Rabi frequency ~400 Hz.

The paper is organized as follows: in Sec. II, we describe our approach to the RF circuit design and its main advantages with respect to more established solutions, and we present the realization of the different components of the RF circuit, namely the coil, the matching network, and the transmission-line transformers; in Sec. III, we report on the characterization of the system performance with an ideal Fermi gas of lithium atoms; in the concluding section, we summarize and provide some outlook.

II. THE CIRCUIT
A. Essentials of atom spin interactions with RF fields

Energy shifts between hyperfine levels of an alkali atom depend on the applied static magnetic field, which sets the quantization direction z, and within the $J = 1/2$ ground-state manifold, they can be precisely computed through the Breit–Rabi formula.[32,33] Since the transitions between hyperfine states or Zeeman sublevels are electric-dipole forbidden, they have an extremely narrow natural linewidth, notably exploited for atomic clocks. External magnetic fields interact with the atom only through the magnetic dipolar interaction.[32,33] In the case of ground-state Zeeman sublevels, the energy splittings for typical B_0 values correspond to RF frequencies ν_0 in the so-called very high frequency (VHF) range, roughly between 10 and 100 MHz, making RF magnetic fields the simplest method to couple different levels with one another.

Let us consider both static and RF magnetic fields that are spatially homogeneous over the scale of the atomic sample, and that the RF field is linearly polarized. We may define the static offset field as $\mathbf{B}_0 = B_0\mathbf{e}_z$, and focus on a pair of adjacent magnetic sublevels, split by an energy $\hbar\omega_0$ associated with B_0. These realize an effective atomic spin-1/2 system, as they coincide with the eigenstates $|m\rangle$ of the spin projection S_z along the quantization axis.[34] The interaction of an atomic spin $\mathbf{S}$ with a RF magnetic field $\mathbf{B}_{RF}(t) = B_{RF}\cos(\omega t + \varphi)\,\hat{e}$ is given by $V_{RF} = g\mu_B B_{RF}\cos(\omega t + \varphi)\,\mathbf{S}\cdot\hat{e}$, where μ_B is the Bohr magneton, g is the relevant gyromagnetic factor,[32] ω and φ are the RF B-field angular frequency and phase offset, and $\hat{e}$ is the field polarization unit vector. To couple the two $|m\rangle$-levels with one another, the RF field polarization must have a non-zero projection in the x–y plane, and its frequency must be close to resonance,[32,33] that is, $\omega \simeq 2\pi\nu_0$. This is the principle behind the phenomenon of nuclear magnetic resonance (NMR). Taking $\hat{e} = \mathbf{e}_y$ to maximize the coupling V_{RF}, without loss of generality, we can define the Rabi frequency $\Omega_R = \mu_\perp B_{RF}/(2\hbar)$. Here, $\mu_\perp$ is the matrix element of the magnetic dipole moment (operator) $\mu_y = g\mu_B S_y$, that is, the transition dipole moment that sets the coupling strength between the two spin states.[26,32,35] The coupling strength of the RF field with an atomic spin is therefore proportional to the magnetic moment component orthogonal to the quantization axis, which in turn depends on the atomic species and the amplitude of the quantization field $\mathbf{B}_0$, and to the amplitude $B_\perp$ of the RF field component orthogonal to the quantization z-axis. The main objective of our circuit design is to maximize the latter quantity for a given set of spatial constraints while minimizing unwanted interference with the surrounding electronic instruments.

B. Design constraints

Atomic physics experiments require a RF B-field having the largest feasible amplitude within the sub-millimeter region of space occupied by the atomic sample. In many setups, atoms are, however, shielded inside a metallic vacuum chamber, which has only a few optical apertures. A pair of reentrant glass viewports located at centimeter-distance from the atoms is often included, to grant large optical access for laser beams and high-resolution imaging optics, representing also the best location where to place large-field electromagnets and a RF field applicator. However, in this configuration, the RF coil becomes coaxial with the Feshbach electromagnets, challenging the requirement that the RF field be orthogonal to their magnetic field. The RF frequency range of atomic hyperfine transitions, for example, $\nu_0 \approx 80$ MHz for the ground-state transitions of lithium atoms, combined with the typical dimensions of the viewports and their distance from the sample, determine working conditions characteristic of magneto-quasistatic fields,[36] that is, slowly oscillating magnetic fields that behave essentially as static. In our apparatus, the reentrant viewports have a diameter of about 60 mm, and their outer glass surfaces are situated at a distance of

20 mm from the sample—to be compared with RF wavelengths of at least a few meters. The standard emitter to generate such a quasistatic field at the near-field location of the atomic sample consists of a small coil of conductive wire. The amplitude B_{RF} in the near field is proportional to the current flowing in such an inductive loop,[36] which must be placed as close as possible to the sample, considering that the field strength of a magnetic dipole decays with the cubed distance.

A possible strategy to minimize the distance between the RF coil and the sample, and to optimally orient the generated B-field polarization $\mathbf{B}_{RF} \perp \mathbf{B}_0$, is to accommodate the coil inside the vacuum chamber. This solution has recently become somewhat more common, but it must be planned ahead of constructing the apparatus. Further, it presents issues with flexibility and tunability, as well as risks of feedthrough and vacuum pressure failures, due to difficult heat management via the vacuum electrical feedthroughs. Therefore, we rather consider a wire loop with a diameter of a few centimeters placed just outside the chamber within one of the reentrant viewports. At the center of the chamber, this will generate only a B-field, the E-field being negligible[37] (and unnecessary). Essentially, the coil transforms the current flowing in it into a B-field; hence, in the ideal case, no energy is dissipated, the only necessary entity being the current itself. Practically, some power is dissipated in the coil itself, in the conductive parts of the vacuum chamber surrounding the coil, and in all resistive elements within the circuit placed between the generator and the coil (e.g., parasitic resistances associated with transmission line losses).
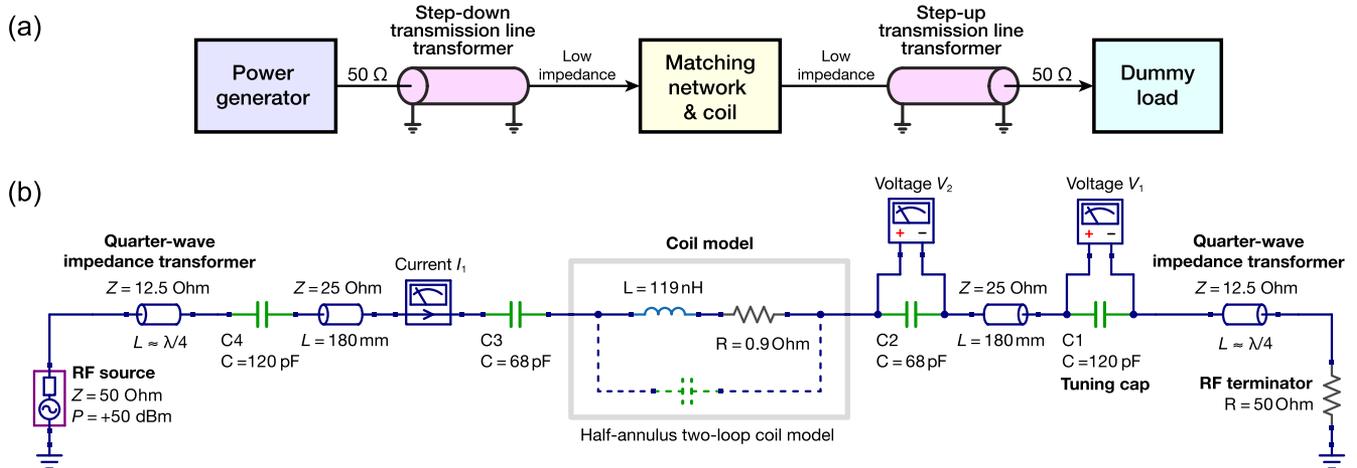
C. Circuit concept and design

A common approach for maximizing the B-field is to maximize the power transfer from the RF generator toward the coil via impedance matching, by interposing a suitable network of elements between the generator and the coil.[38–40] However, a coil with such small dimensions has only a tiny radiation resistance of (at most) a few tens of mΩ for VHF frequencies, much smaller than its own loss resistance on the order of 1 Ω, and negligible with respect to the 50 Ω output impedance of the generator. Matching the impedance of the generator is thus particularly challenging, since the widely different loads entail very high currents and voltages across the LC elements of the interposed matching network, leading to power losses.[41] In addition, since the matching network must be placed at the location of the coil to avoid that the feedline becomes part of the field-emitter itself, it is highly impractical to adjust the resonant frequency of the circuit, since this location is typically not accessible after the installation in the experimental setup.

Rather than attempting to directly match the coil impedance to the 50 Ω output impedance of the generator,[42] here we adopt a different strategy that upscales the current flowing through the coil, while avoiding high voltages across matching elements and minimizing radiation from the feedline. The essential idea is to integrate the coil into a transmission line with a low controlled impedance using an impedance transformer, to achieve a high current level in the coil while avoiding large power dissipation through its parasitic losses. Importantly, this approach avoids introducing any unbalanced line segments that would emit unwanted RF fields. This is essential for stable operation and minimizing electromagnetic interference with the experimental instrumentation.

To realize this scheme, we design a setup consisting of a series of elements that work together to form an optimized impedance transformation system. The RF generator, which has an output impedance of 50 Ω, is connected to a step-down impedance transformer that significantly reduces the impedance seen by the coil. Immediately after the step-down transformation, a matching network is introduced to interface the impedance of the coil with the rest of the circuit through a tuning board. This board also ensures that the system operates at the desired resonance frequency, enabling fine-tuning of the frequency response without requiring physical modifications in the vicinity of the coil. Following the coil, a step-up impedance transformer is used to restore the impedance back to 50 Ω, allowing the majority of the power to be dissipated in a dummy load, rather than mainly in the coil as it would happen by connecting the latter directly to ground. While the 50 Ω resistive load decreases the power transferred to the coil and thus the current by a factor of almost 2, it is fundamental to balance the network design, avoiding common-mode currents on the ground return path that would cause unwanted radiation from the cable connecting the RF generator to the step-down transformer. Indeed, with an unbalanced network, the transmission-line section located upstream of the first step-down transformer, between the RF generator and the step-down transformer itself, would feature different currents flowing on the inner conductors and the (grounded) shield and would thus radiate efficiently, having a length of tens of centimeters, comparable with radio wavelengths in the VHF range. The main blocks of our circuit design are illustrated in Fig. 1(a).

Several approaches exist to transforming a transmission line impedance, including the use of ferrite-loaded binocular transformers and stub-loaded line transformers.[41] We adopt a quarter-wave coaxial line transformer due to its effectiveness in achieving a high impedance transformation ratio while maintaining simplicity and robustness. In addition, the quarter-wave transformer is particularly suitable for our application because it does not introduce ferromagnetic materials, which would interfere with the high static magnetic fields used in ultracold-atom experiments for interaction tuning, creating uncontrolled magnetic disturbances to the atomic levels. The quarter-wave transformer is a narrowband solution, but it is fully compatible with a typical tunability range of a few MHz required to address the atomic resonance at $\nu_0 = \omega_0/2\pi$ for different values of the external magnetic field B_0—e.g., $\nu_0 = 81$–85 MHz for the $|2\rangle \leftrightarrow |3\rangle$ transition of ^{6}Li. Moreover, the proposed approach can yield a large amplification of the current flowing through the coil, depending on the choice of the quarter-wave transformer ratio. This solution also guarantees the reproducibility of the performance of the antenna due to its mechanical and electrical stability, reducing the need for later adjustments.

Summarizing the main benefits of the proposed design: (i) it provides a significant enhancement of the current flowing through the coil for a given available power from the generator, ensuring access to the strong RF driving regime of atomic transitions; (ii) it allows for straightforward frequency adjustments through a single accessible low-voltage component, facilitating experimental fine-tuning *in situ*; (iii) it minimizes RF interference and ensures compliance with electromagnetic compatibility (EMC) requirements, reducing the risk of unintended radiation affecting other laboratory equipment; (iv) it simplifies the overall circuit construction, making it easily adaptable to similar experimental setups.

FIG. 1. Circuit concept and design. (a) A block diagram displays the five cascaded components composing the RF circuit: the generator, the step-down transformer, the matching network that compensates the coil impedance, the step-up transformer, and the 50 Ω dummy load. (b) Full layout of the RF circuit. The step-down and step-up transformers are implemented by quarter-wave 12.5 Ω coaxial transmission lines. They respectively decrease and increase the impedance of their "secondary" sides by a factor of 16. The coil is modeled as a LR series, based on impedance measurements of the actual wire loop (see Fig. 2) inserted in a mock-up of the vacuum chamber. The capacitors compose the matching network together with the two 180-mm-long transmission lines bridging the tuning board and the coil (see also Fig. 4). The capacitance values shown here apply to a central frequency around 83 MHz.

D. The coil

A high B-field can be obtained with a coil consisting of several turns, but the self-inductance rises with the square of the number of turns. High values of the self-inductance yield a reactance that is difficult to compensate. In addition, as described previously, only the generated field component oriented orthogonally to the atom quantization axis z couples to the atomic spin, that is, $\mathbf{B}_\perp \perp \mathbf{B}_0$. Since $\mathbf{B}_0$ is produced by strong electromagnets also installed in the reentrant viewports, z is perpendicular to the viewport surface. We have considered a variety of three-dimensional asymmetric coil geometries, ranging from tilted ellipses to off-centered asymmetric or twisted profiles. We have assessed their performance in simulations by quantifying: (i) the magnitude of the B-field component $B_\perp$ to maximize the Rabi frequency; (ii) the homogeneity of such transverse $B_\perp$ field around the location of the atomic sample to minimize spatial dephasing over extended atomic samples; (iii) the clearance along the z-axis at $x, y = 0$ to maximize optical access to the atomic sample.

The best trade-off was found with a two-turn loop shaped as a half-annulus, as depicted in Fig. 2(a), reminiscent of previously reported kidney-shaped loops.[39,43] This planar coil geometry maximizes the field component orthogonal to $\mathbf{e}_z$ [see Fig. 2(b)] for the fixed minimum distance d between the atoms' location and the coil, $|d| \simeq 0.7 R_{ext}$. In particular, at the atoms' location, the simulation estimates a magnetic field component $B_\perp \approx 0.05$ G/A_{pp} and an angle of ~70° between the field and the z-axis (see Appendix). This angle becomes 90° at a distance of about half of the coil's external radius, which is, however, incompatible with our coil external radius and distance-to-atoms constraints. Moreover, the generated field is nearly homogeneous over several millimeters around the atomic sample location [see Fig. 2(b)], rendering the design robust to manufacturing imperfections. The coil has been realized using

the same coaxial cable used for transmission-line transformers (see the next paragraph). Using coaxial cable is not essential, as RF currents flow only on the braid and the central conductor is inactive, but it simplifies the construction and makes it reliable even for high powers.

## E. Circuit implementation and simulation

The circuit is implemented according to the schematic in Fig. 1(b). Figure 3 shows a simulation of the whole circuit carried out with the Qucs software,[44] which guided the choice of the actual components and parameters. To match the impedance from 50 Ω (generator) to a lower value suitable to increase the current in the coil, a $\lambda/4$ transmission-line transformer[41] has been used. The relationship between the characteristic impedance of the line Z_0, and the impedances seen at the input side Z_{in} and output side Z_{out} of the transformer is given by

$$Z_{out} = \frac{Z_0^2}{Z_{in}}. \tag{1}$$

Thus, to have a large impedance variation toward lower values, it is necessary to have low-impedance transmission lines. Lines with characteristic impedance between 10 and 75 Ω are available, but for simplicity, we have chosen to use only 25 Ω coaxial cables. Using two 25 Ω coaxial cables in parallel (or equivalently four 50 Ω cables) has approximately the same effect as using a single 12.5 Ω cable, with the added advantage of power sharing between different cables, such that small ones can be used. With this choice, the impedance seen after the transformer toward the generator is 3.125 Ω, namely 16 times lower than the original value. More dramatic impedance reductions are feasible by adding further cables in parallel until
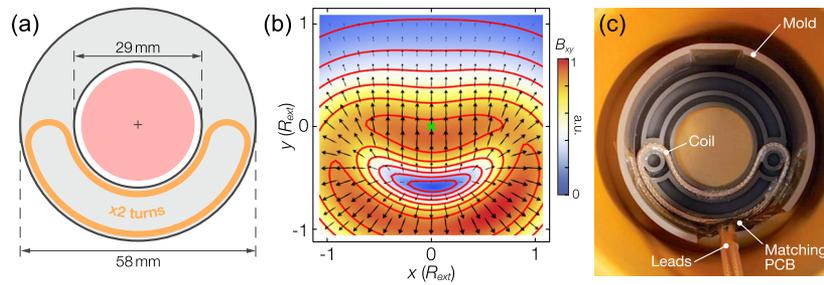
FIG. 2. Coil design and realization. (a) The coil is formed by two turns of a half-annulus shaped coaxial wire loop (orange line), with an external radius $R_{ext} \simeq 29$ mm. A clear optical aperture of 29 mm diameter, centered on the viewport remains available, used, for example, to shine a 25.4 mm-diameter beam on the atoms (pink circle). (b) Calculated B-field polarization pattern and transverse component amplitude $B_{\perp}$ in the atomic plane at $z \simeq 0.7R_{ext} \simeq 20$ mm. The in-plane component $B_{\perp}$ is dominant and quite homogeneous around the sample location $x, y = 0$ (green cross). In particular, at the largest contour line, that delimits a region of about 30×10 mm^2, $B_{\perp}$ is reduced by only 15% with respect to its value at the atoms' position. (c) The coil has been realized using coaxial RG316 cable, and is held in shape by a 3D-printed supporting mold (gray plastic cylinder with grooves). The two lead cables visible in the bottom part of the picture connect to the coil through two capacitors C2 and C3 soldered to a centimeter-sized PCB [see Fig. 4(a)]. Measurements of the coil impedance are performed for simulation purposes, surrounding it with a metallic cylinder to emulate the EM environment within the reentrant viewport.
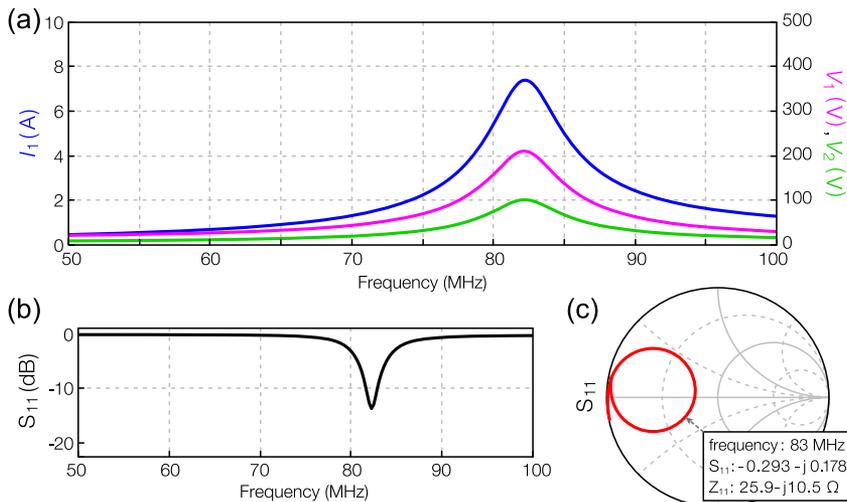
FIG. 3. Circuit simulation results for a 100 W generator, calculated based on the components displayed in Fig. 1(b). (a) The current (peak-to-peak) I_1 in the coil (blue), and the voltages (peak-to-peak) V_1 (magenta) and V_2 (green) across the matching capacitors C1 and C2, respectively, are displayed. (b) and (c) The modulus and Smith chart of the circuit S_{11} parameter are shown, quantifying the power reflected back to the generator.

parasitic resistances of a few 100 mΩ of the coil (skin effect) and solder connections may become a limiting factor.

The matching network, which includes series capacitors and 25 Ω coaxial cables and incorporates the coil, serves to cancel the inductive reactance of the coil itself. The 25 Ω cable sections also facilitate the installation and the manual capacitance tuning in the intricate environment close to the experimental chamber. After the last (tunable) capacitor C1, another $\lambda/4$ transformer raises the impedance again from 3.125 to 50 Ω, matching that of the terminating load. As can be seen from simulations shown in Fig. 3(a), in addition to good matching over a relatively wide frequency bandwidth (FWHM) of about 10 MHz, the current I_1 is enhanced by a factor $\eta \simeq (Z_{in}/\tilde{Z}_{out})^{1/2} \lesssim 4$ with respect to the current that would be obtained using a generator transferring the same power onto a generic 50 Ω load (e.g., 2 A$_{pp}$ for a 100 W generator). Here,

$\tilde{Z}_{out} \gtrsim 3.125$ Ω denotes the impedance seen at the output side of the step-down transformer taking also into account the 180-mm-long transmission-line section.

The other graphs show the voltages V_1 and V_2 across capacitors C1 and C2, which are well below the maximum working voltage of ceramic capacitors such as the ATC 100B series and air dielectric trimmers. With respect to the well-established approach of L-matching the coil impedance by creating a resonant LC network, our design improves the bandwidth by more than a factor of 2 while considerably reducing the voltage across the matching capacitor, at the cost of a lower Q-factor (by a factor less than 2). In our simulations, the coil has been modeled as a LR series, whose values are based on vector impedance measurements of the actual coil build [see Fig. 2(c)]. Given the low RF frequencies involved and the small dimensions, no parasitic resonance was observed, so the

model turned out to be particularly simple—no parallel capacitance is included. As described in the following paragraphs, measurements and simulations are in close agreement.

F. Realization

Figure 4(a) shows a sketch of the realized circuit. We opted to add an extra transmission-line section of 180 mm length to reach the vacuum viewport of the experiment while keeping the tuning capacitor C1 at reach. The system is built using a $Z_0 = 25$ Ω coaxial cable (QAXIAL RG316/25-FLEX) with non-magnetic conductors and high-power handling of ~500 W at 80 MHz, and high-voltage porcelain multilayer SMD capacitors from American Technical Ceramics (ATC 100B series, non-magnetic). All ATC capacitors are able to withstand 1 kV and have a Q-factor exceeding 1000 at 100 MHz. To hold the coil in shape, a rigid plastic support has been realized with a 3D printer [see Fig. 2(c)], increasing the robustness of the system and facilitating the insertion of the coil into the vacuum viewport mechanical clearance. The step-down and step-up transformers are realized using two couples of 620-mm-long coaxial sections, corresponding to $\lambda/4$ segments at 80 MHz. The matching network includes [see Fig. 4(b)] (i) capacitors C2 and C3, used to create a matching between the loop and the line; (ii) a pair of coaxial cables with characteristic impedance $Z_0 = 25$ Ω which link the C2/C3 board to the tuning board; (iii) capacitors C1 and C4, realized with 2 fixed capacitors and a tunable trimmer capacitor, necessary for finely tuning the resonance frequency. The latter is implemented by an air

dielectric trimmer capacitor from Johanson Technology, with a voltage rating of 500 V, a capacitance range of 1–30 pF and a Q-factor >800 at 100 MHz.

III. CIRCUIT PERFORMANCE

A. Electrical network measurements

The measurement phase started with the characterization of the coil impedance to determine the actual L and R parameters to input into the circuit model. The matching network has been designed, realized, and tested on the workbench. Subsequently, the coil has been inserted into the viewport, and the complete system tested *in situ*. Illustrative measurements performed with a vector network analyzer (VNA) are shown in Figs. 4(c)–4(d). The circuit resonant frequency can be shifted over a range of about 2 MHz by varying the value of C4 by 30 pF without visibly reducing the impedance matching. For a given resonance position, the current bandwidth, defined as the full width at half maximum (FWHM) of the current resonance, equals ~10 MHz [see Fig. 3(a)].

B. Testing the system on atomic samples

We have tested the system in our experiment with ultracold degenerate gases of fermionic lithium atoms.[2,21] We have addressed the transition between the second-lowest and third-lowest magnetic sublevels of ^{6}Li ground state, usually labeled $|2\rangle$ and $|3\rangle$, respectively. In the experiment, offset fields in the range $B_0 \simeq 570$–900 G are used,[2] covering the position of two broad Feshbach resonances
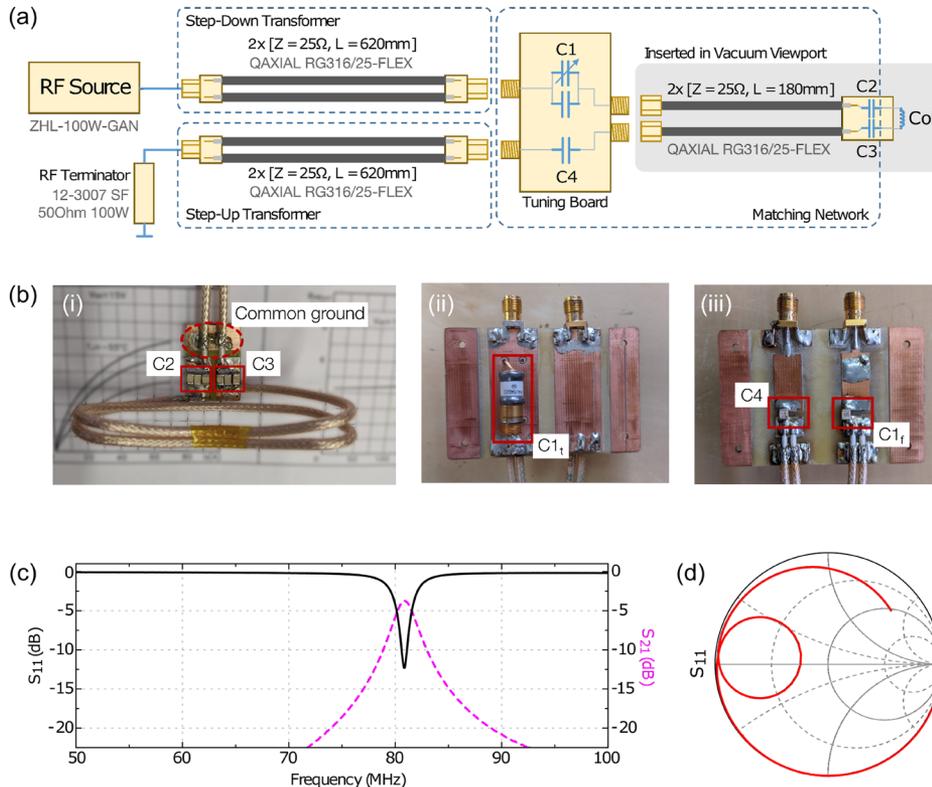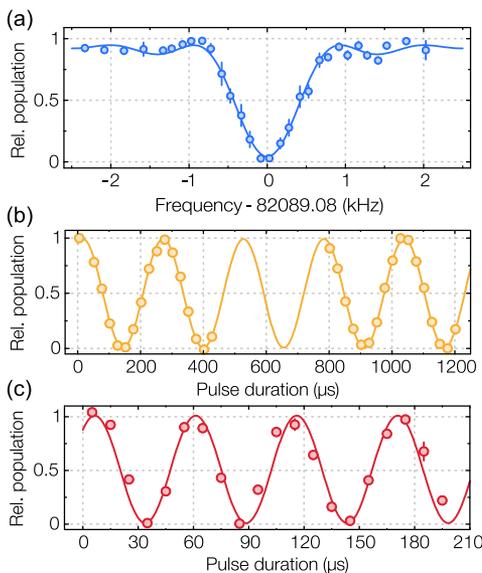

FIG. 4. Circuit realization and *in situ* measurements. (a) Sketch of the circuit boards and components. (b) Pictures of the realized matching (and tuning) network board. Capacitors C2 and C3 are hosted by a cm-sized PCB mounted vertically next to the coil within the plastic housing [see Fig. 2(c)]. The two coaxial cables connecting the tuning board with C2 and C3 share a common ground, preventing B-fields from being emitted at any other location on the feedline than the loop itself. Capacitors C1 and C4 are soldered on a dedicated PCB, which is housed and fixed to a breadboard outside the reentrant viewport. The tuning capacitance is realized by two capacitors C1$_f$ (fixed) and C1$_t$ (trimmer), C1 = C1$_f$ + C1$_t$. All fixed capacitors are ATC-100B series, while the tuning capacitance in C1 is realized with a Johanson MAV05D30. (c) and (d) The S_{11} parameter measured with a vector network analyzer is found in good agreement with simulations [see Fig. 3(c)]. The S_{21} parameter quantifies the power reaching the final 50 Ω load and equals about −3 dB at the resonance (here $\simeq 81$ MHz).

at 690 and 832 G between states $|2\rangle$ and $|3\rangle$, and the lowest hyperfine level $|1\rangle$. For such B_0 values, nuclear and electron spins of the atom are largely decoupled,[32,45] and the spin system formed by states $|2\rangle$ and $|3\rangle$ has a small magnetic moment $|\mu_\perp|/h \lesssim 70$ kHz/G (still much larger than the nuclear magnetic moment $\mu_N \simeq \mu_B/1836$, with $\mu_B/h \simeq 1.4$ MHz/G).

A spectroscopic measurement of the $|2\rangle \leftrightarrow |3\rangle$ transition in an ideal (spin-polarized) degenerate Fermi gas at $B_0 \simeq 770$ G is displayed in Fig. 5(a). A sinc-shaped line centered around 82 MHz is observed, associated with the 1 ms-long square pulse at 50 mW of RF power, used for the spectroscopic transfer shown here. A spectral stability below 100 Hz is observed during the several minutes necessary for a full spectroscopic measurement, corresponding to an offset B-field stability below 10 mG, or a fractional stability around 10^{-5}.

To benchmark the performance of our RF system at high power, we have performed Rabi oscillation measurements at the measured resonance of the $|2\rangle \leftrightarrow |3\rangle$ transition. Illustrative results are displayed in Figs. 5(b) and 5(c), where a coherent sinusoidal evolution of the state populations is visible for two different driving powers. The intrinsic lifetime of the hyperfine states is much longer than the typical measurement time scales, guaranteeing that visible damping originates only from dephasing from temporal magnetic field fluctuations or spatial inhomogeneities over the atomic sample. Since no measurable damping is observed during the evolution, we conclude that our RF setup does not significantly influence

the surrounding electronic equipment, used to actively stabilize the value of B_0 (comprised of current transducers, analog PID loops, and DC regulated power supplies) over the typical timescale of the experiment for each RF power. Extracting the Rabi frequency with a sinusoidal fit to the data, we find $\Omega_R/2\pi \simeq 18.25$ kHz for a driving power of about 80 W. This corresponds to a π-pulse duration of 27.5 μs, which is on the order of the Fermi time $\tau_F \simeq 30$ μs in our degenerate Fermi gas. The measured Rabi frequency yields a coupling B-field of 0.29 G, in good agreement with the simulation predictions of 0.32 G.

IV. CONCLUSIONS

In this paper, we have described a practical approach to the generation of strong, quasistatic ~100 MHz RF magnetic fields for atomic physics experiments. This provides an efficient, low-cost, and uncomplicated solution to achieve large coupling strengths with atomic spins without introducing detrimental disturbances or reliability issues. The realized circuit is able to withstand short pulses with RF power $P > 100$ W, further increasing the maximum attainable B-field amplitudes and atomic Rabi frequencies. Alternatively, larger current enhancement factors η could be obtained by implementing higher impedance-transformer ratios η^2, for example, $\eta = 6$ would allow us to achieve the same maximum Rabi frequency demonstrated here by using a ~40 W generator.

Our design can be straightforwardly adapted to other alkali atomic species such as K, Rb, or Na. Recently, it has been extended to address the RF transition at ~240 MHz in Cr atoms,[46] demonstrating the feasibility of our approach even at frequencies beyond the magneto-quasistatic regime.[47,48] Moreover, our scheme is flexible against optical apertures or positioning constraints, possibly also for in-vacuum RF coils, where tilted or deformed circular loops may be considered. We believe our system may become a standard solution for RF field coupling to alkali atom spins in current and forthcoming experimental setups, where large optical access and modularity have become a must.

Note added in proof. After the first release of this manuscript in the arXiv repository, our circuit design and coil profile have been extended in Ref. 49 to the low-frequency regime (~30 MHz). In this adapted version, the field-emitting coil also serves as the inductive element within a low-loss capacitive transformer, which entirely replaces the step-down quarter-wave transformer in our design.

FIG. 5. System performance measured with an ideal Fermi gas of ^{6}Li atoms at $B_0 \simeq 770$ G. On the vertical axis, the relative population denotes the number of atoms in state $|2\rangle$ normalized to the total atom number. (a) Spectroscopy of the $|2\rangle \leftrightarrow |3\rangle$ transition. The solid line is a fit of the data with the expected sinc-function line shape, yielding a resonance frequency $\nu_0 = 82.089\,08(1)$ MHz and a Rabi frequency $\Omega_R/2\pi = 410(16)$ Hz. (b) and (c) Rabi oscillations at the resonance between states $|2\rangle$ and $|3\rangle$ for RF generator powers of about 3.5 W (yellow) and 80 W (red). Solid lines are sinusoidal fits to the data, yielding Rabi frequencies $\Omega_R/2\pi = 3.909(4)$ kHz and $\Omega_R/2\pi = 18.25(23)$ kHz, respectively.

program HORIZON-CL4-2022-QUANTUM-02-SGA via Project No. 101113690 (PASQuanS2.1).

AUTHOR DECLARATIONS

Conflict of Interest

The authors have no conflicts to disclose.

Author Contributions

F. Scazza: Conceptualization (equal); Data curation (equal); Formal analysis (equal); Investigation (equal); Methodology (equal); Supervision (equal); Writing – original draft (equal); Writing – review & editing (equal). **G. Del Pace**: Conceptualization (equal); Data curation (equal); Formal analysis (equal); Investigation (equal); Methodology (equal); Supervision (equal); Writing – original draft (equal); Writing – review & editing (equal). **L. Pieri**: Conceptualization (equal); Formal analysis (equal); Investigation (equal); Methodology (equal); Writing – original draft (equal). **R. Concas**: Conceptualization (equal); Formal analysis (equal); Investigation (equal); Methodology (equal); Writing – review & editing (equal). **W. J. Kwon**: Funding acquisition (equal); Investigation (equal); Methodology (equal); Project administration (equal); Supervision (equal); Writing – review & editing (equal). **G. Roati**: Funding acquisition (equal); Investigation (equal); Methodology (equal); Project administration (equal); Supervision (equal); Writing – review & editing (equal).

DATA AVAILABILITY

The data that support the findings of this study are available from the corresponding author upon reasonable request.

APPENDIX: SIMULATED B-FIELD PROFILE

In this section, we provide further details on the simulations that we performed to optimize the coil shape. Our simulations account for the real shape of the coil (including the finite volume of the wire loops), identifying the half-annulus design as the best trade-off considering the criteria mentioned in Sec. II D. Such a solution offers a clear shape prescription, which is easy to reproduce and adapt to different absolute dimensions. The field-generating performance remains optimal as long as the target field location lies at $(x, y) \simeq (0, 0)$ and $|z| \in [0.5R_{\text{ext}}, 0.7R_{\text{ext}}]$, see Fig. 6. Here, $(x, y, z) = (0, 0, 0)$ refers to the center of the annulus in the mid-plane of the coil itself.

The simulated transverse B-field magnitude at the atoms' location, $(x, y, z) \simeq (0, 0, |d|)$, equals $B_\perp \approx 0.05$ G/A$_{\text{pp}}$. The axial B-field at the same location is estimated as $B_z \leq 0.4B_\perp$, corresponding to a field angle with respect to the x–y plane of about $22°$. Decreasing the distance from the atoms to the emitter by around 5 mm would completely zero the axial B_z component, also yielding a moderate
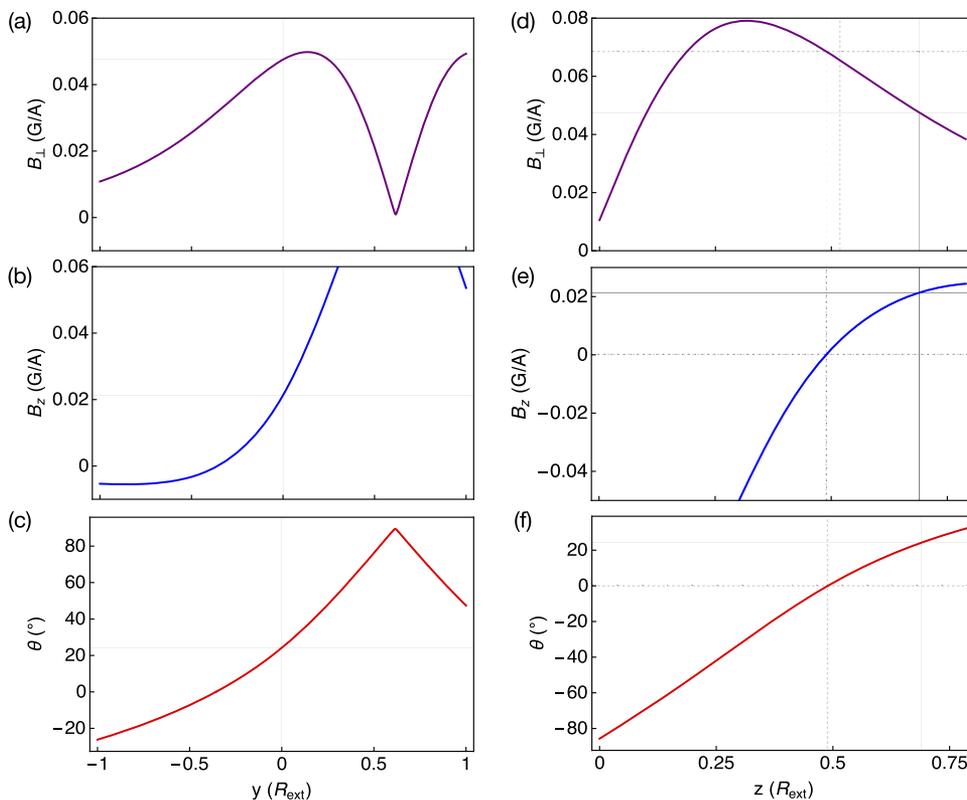
FIG. 6. Simulated spatial profile of the B-field generated by the RF coil for a current of 1 A$_{\text{pp}}$ flowing through the coil. (a) and (b) Transverse and axial RF-field amplitudes, $B_\perp$ and B_z, along the y-axis at $(x, z) = (0, |d|)$. (c) B-field vector angle with respect to the x–y plane along the y-axis. (d) and (e) Transverse and axial RF-field amplitudes, $B_\perp$ and B_z, along the z-axis at $(x, y) = (0, 0)$. (f) B-field vector angle with respect to the x–y plane along the z-axis. The position of the atomic sample is $(x, y, z) \simeq (0, 0, |d|)$ with $|d| \simeq 0.7R_{\text{ext}}$, as denoted by solid vertical grid lines. Dashed vertical grid lines denote the optimal coil distance from the atomic sample to obtain a B-field perpendicular to the z-axis at $(x, y) = (0, 0)$.

increase of the useful field $B_\perp \approx 0.068$ G/A_{pp}. This indicates that an optimal ratio of sample distance to coil annulus external radius is realized for $|d|/R_{ext} \approx 0.5$. However, this ratio is incompatible with the constraints of our vacuum chamber, and the smallest achievable ratio in our case is around 0.68, that is, $|d| \approx 20$ mm.

The simulated values for the transverse B-field generated by the coil match reasonably well the values obtained experimentally, which can be extracted from the atomic Rabi frequencies measured, shown in Sec. III B, by calculating the magnetic dipole moment $\mu_\perp \approx 70$ kHz/G of the lithium $2 \leftrightarrow 3$ hyperfine transition. For 80 and 3.5 W, we measure Rabi frequencies of 18.3 and 3.9 kHz, respectively. These values correspond to coupling B-fields of 0.29 and 0.056 G, respectively, to be compared to simulation predictions of 0.32 and 0.07 G.

REFERENCES

[1] M. Inguscio and L. Fallani, *Atomic Physics: Precise Measurements and Ultracold Matter* (Oxford University Press, 2013).

[2] W. Ketterle and M. Zwierlein, *Proceedings of the International School of Physics "Enrico Fermi," Course CLXIV, Varenna, 20–30 June 2006* (IOS Press, Amsterdam, 2008).

[3] M. Inguscio, W. Ketterle, S. Stringari, and G. Roati (Eds.), *Quantum Matter at Ultralow Temperatures* (IOS Press, Amsterdam, 2016).

[4] P. Törmä, "Physics of ultracold Fermi gases revealed by spectroscopies," Phys. Scripta **91**, 043006 (2016).

[5] C. J. Vale and M. Zwierlein, "Spectroscopic probes of quantum gases," Nat. Phys. **17**, 1305 (2021).

[6] C. Chin, M. Bartenstein, A. Altmeyer, S. Riedl, S. Jochim, J. H. Denschlag, and R. Grimm, "Observation of the pairing gap in a strongly interacting Fermi gas," Science **305**, 1128 (2004).

[7] J. T. Stewart, J. P. Gaebler, and D. S. Jin, "Using photoemission spectroscopy to probe a strongly interacting Fermi gas," Nature **454**, 744 (2008).

[8] A. Schirotzek, C.-H. Wu, A. Sommer, and M. W. Zwierlein, "Observation of Fermi polarons in a tunable Fermi liquid of ultracold atoms," Phys. Rev. Lett. **102**, 230402 (2009).

[9] C. Kohstall, M. Zaccanti, M. Jag, A. Trenkwalder, P. Massignan, G. M. Bruun, F. Schreck, and R. Grimm, "Metastability and coherence of repulsive polarons in a strongly interacting Fermi mixture," Nature **485**, 615 (2012).

[10] M. Koschorreck, D. Pertot, E. Vogt, B. Fröhlich, M. Feld, and M. Köhl, "Attractive and repulsive Fermi polarons in two dimensions," Nature **485**, 619 (2012).

[11] F. Scazza, G. Valtolina, P. Massignan, A. Recati, A. Amico, A. Burchianti, C. Fort, M. Inguscio, M. Zaccanti, and G. Roati, "Repulsive Fermi polarons in a resonant mixture of ultracold ^{6}Li atoms," Phys. Rev. Lett. **118**, 083602 (2017).

[12] M.-G. Hu, M. J. Van de Graaff, D. Kedar, J. P. Corson, E. A. Cornell, and D. S. Jin, "Bose polarons in the strongly interacting regime," Phys. Rev. Lett. **117**, 055301 (2016).

[13] N. B. Jørgensen, L. Wacker, K. T. Skalmstang, M. M. Parish, J. Levinsen, R. S. Christensen, G. M. Bruun, and J. J. Arlt, "Observation of attractive and repulsive polarons in a Bose–Einstein condensate," Phys. Rev. Lett. **117**, 055302 (2016).

[14] Z. Z. Yan, Y. Ni, C. Robens, and M. W. Zwierlein, "Bose polarons near quantum criticality," Science **368**, 190 (2020).

[15] J. Etrych, G. Martirosyan, A. Cao, C. J. Ho, Z. Hadzibabic, and C. Eigen, "Universal quantum dynamics of Bose polarons," Phys. Rev. X **15**, 021070 (2025).

[16] Y. Sagi, T. E. Drake, R. Paudel, and D. S. Jin, "Measurement of the homogeneous contact of a unitary Fermi gas," Phys. Rev. Lett. **109**, 220402 (2012).

[17] B. Mukherjee, P. B. Patel, Z. Yan, R. J. Fletcher, J. Struck, and M. W. Zwierlein, "Spectral response and contact of the unitary Fermi gas," Phys. Rev. Lett. **122**, 203402 (2019).

[18] R. J. Fletcher, R. Lopes, J. Man, N. Navon, R. P. Smith, M. W. Zwierlein, and Z. Hadzibabic, "Two- and three-body contacts in the unitary Bose gas," Science **355**, 377 (2017).

[19] A. B. Bardon, S. Beattie, C. Luciuk, W. Cairncross, D. Fine, N. S. Cheng, G. J. A. Edge, E. Taylor, S. Zhang, S. Trotzky, and J. H. Thywissen, "Transverse demagnetization dynamics of a unitary Fermi gas," Science **344**, 722 (2014).

[20] M. Cetina, M. Jag, R. S. Lous, I. Fritsche, J. T. M. Walraven, R. Grimm, J. Levinsen, M. M. Parish, R. Schmidt, M. Knap, and E. Demler, "Ultrafast many-body interferometry of impurities coupled to a Fermi sea," Science **354**, 96 (2016).

[21] A. Amico, F. Scazza, G. Valtolina, P. E. S. Tavares, W. Ketterle, M. Inguscio, G. Roati, and M. Zaccanti, "Time-resolved observation of competing attractive and repulsive short-range correlations in strongly interacting Fermi gases," Phys. Rev. Lett. **121**, 253602 (2018).

[22] M. G. Skou, T. G. Skov, N. B. Jørgensen, K. K. Nielsen, A. Camacho-Guardian, T. Pohl, G. M. Bruun, and J. J. Arlt, "Non-equilibrium quantum dynamics and formation of the Bose polaron," Nat. Phys. **17**, 731 (2021).

[23] F. J. Vivanco, A. Schuckert, S. Huang, G. L. Schumacher, G. G. T. Assumpção, Y. Ji, J. Chen, M. Knap, and N. Navon, "The strongly driven Fermi polaron," Nat. Phys. **21**, 564 (2025).

[24] W. Ketterle and N. J. V. Druten, "Evaporative cooling of trapped atoms," in *Advances in Atomic, Molecular, and Optical Physics*, edited by B. Bederson and H. Walther (Academic Press, 1996), Vol. 37, pp. 181–236.

[25] S. Hofferberth, I. Lesanovsky, B. Fischer, J. Verdu, and J. Schmiedmayer, "Radiofrequency-dressed-state potentials for neutral atoms," Nat. Phys. **2**, 710 (2006).

[26] H. Perrin and B. M. Garraway, "Trapping atoms with radio frequency adiabatic potentials," in *Advances in Atomic, Molecular, and Optical Physics*, edited by E. Arimondo, C. C. Lin, and S. F. Yelin (Academic Press, 2017), Vol. 66.

[27] B. Braverman, A. Kawasaki, E. Pedrozo-Peñafiel, S. Colombo, C. Shu, Z. Li, E. Mendez, M. Yamoah, L. Salvi, D. Akamatsu, Y. Xiao, and V. Vuletić, "Near-unitary spin squeezing in ^{171}Yb," Phys. Rev. Lett. **122**, 223203 (2019).

[28] S. Ma, A. P. Burgers, G. Liu, J. Wilson, B. Zhang, and J. D. Thompson, "Universal gate operations on nuclear spin qubits in an optical tweezer array of ^{171}Yb atoms," Phys. Rev. X **12**, 021028 (2022).

[29] R. Schmidt, M. Knap, D. A. Ivanov, J.-S. You, M. Cetina, and E. Demler, "Universal many-body response of heavy impurities coupled to a Fermi sea: A review of recent progress," Rep. Prog. Phys. **81**, 024401 (2018).

[30] H. S. Adlong, W. E. Liu, F. Scazza, M. Zaccanti, N. D. Oppong, S. Fölling, M. M. Parish, and J. Levinsen, "Quasiparticle lifetime of the repulsive Fermi polaron," Phys. Rev. Lett. **125**, 133401 (2020).

[31] F. Scazza, M. Zaccanti, P. Massignan, M. M. Parish, and J. Levinsen, "Repulsive Fermi and Bose polarons in quantum gases," Atoms **10**, 55 (2022).

[32] D. A. Steck, Quantum and atom optics (revision 0.13.4), 2020.

[33] B. H. Bransden and C. J. Joachain, *Physics of Atoms and Molecules* (Pearson Education, 2003).

[34] While the considered spin **S** typically maps to the total angular momentum **F** of the hyperfine atomic state, in the limit of large magnetic fields B_0 it approaches the nuclear spin **I**, which decouples from the electronic shell.[33]

[35] Note that in general both the transition dipole moment $\mu_\perp$ and the differential Zeeman shift $\delta\mu_\parallel$ of the two spin states depend on the magnetic dipole operator and on the quantization field amplitude B_0. However, while $\mu_\perp$ is the off-diagonal matrix element of the magnetic dipole operator evaluated between the two atomic states, $\delta\mu_\parallel$ is the difference between the expectation values of the longitudinal component of the magnetic dipole $\mu_z = g\mu_B S_z$, parallel to the quantization field **B**$_0$.

[36] H. A. Haus and J. R. Melcher, *Electromagnetic Fields and Energy* (Prentice Hall, Englewood Cliffs, NJ, 1989), Vol. 107.

[37] In such near-field quasistatic condition, it is indeed inappropriate to refer to the emitter as an "antenna," since the propagating electromagnetic radiation is irrelevant, and we will henceforth refer to it simply as the "coil."

[38] A. N. Wenz, "Few-body physics in a three-component Fermi gas," M.S. thesis, University of Heidelberg, 2009.

[39] D. Mitra, "Exploring attractively interacting fermions in 2D using a quantum gas microscope," Ph.D. thesis, University of Princeton, 2018.

[40] Z. A. Geiger, "An apparatus for dynamical quantum emulation using ultracold lithium," Ph.D. thesis, University of California, Santa Barbara, 2018.

[41] R. E. Collin, *Foundations for Microwave Engineering* (John Wiley & Sons, 2007).

[42] D. S. Barker, A. Restelli, J. A. Fedchak, J. Scherschligt, and S. Eckel, "A radiofrequency voltage-controlled current source for quantum spin manipulation," Rev. Sci. Instrum. **91**, 104708 (2020).

[43] T. Lompe, "Efimov physics in a three-component Fermi gas," Ph.D. thesis, University of Heidelberg, 2011.

[44] Available under GPL license at http://qucs.sourceforge.net.

[45] M. E. Gehm, *Preparation of an optically-trapped Degenerate Fermi Gas of ^6Li: Finding the Route to Degeneracy* (Duke University, 2003).

[46] A. Cosco, "Optimized production and probing of resonantly interacting lithium-chromium Fermi mixtures," M.S. thesis, University of, Florence, 2022.

[47] For frequencies exceeding 200 MHz, the RF coil features a typical radiation resistance around 1 Ω, and its behavior crosses over to that of a small-loop antenna,[48] for which the radiated power becomes significant.

[48] J. Kraus, *Antennas* (McGraw-Hill, 1988).

[49] Y. Wei, Z. Hu, Y. Guo, Z. Qian, S. Jin, X. Chen, and X.-j. Liu, "A radiofrequency emitter design for the low-frequency regime in atomic experiments," arXiv:2502.11549 (2025).

18 December 2025 00:36:40